

Banner appropriate to article type will appear here in typeset article

Spinning Twisted Ribbons: When Two Holes Meet on a Curved Liquid Film

Jack H. Y. Lo¹†, Yuan Liu¹, Tariq Alghamdi², Muhammad F. Afzaal¹ and Sigurdur T. Thoroddsen¹†

¹Division of Physical Sciences and Engineering, King Abdullah University of Science and Technology (KAUST), Thuwal 23955-6900, Saudi Arabia

²Mechanical Engineering Department, College of Engineering and Architecture, Umm Al-Qura University, Makkah 21955, Saudi Arabia

(Received xx; revised xx; accepted xx)

The rupture of a liquid film, where a thin liquid layer between two other fluids breaks and forms holes, commonly occurs in both natural phenomena and industrial applications. The post-rupture dynamics, from initial hole formation to the complete collapse of the film, are crucial because they govern droplet formation, which plays a significant role in many applications such as disease transmission, aerosol formation, spray drying nanodrugs, oil spill remediation, inkjet printing, and spray coating. While single-hole rupture has been extensively studied, the dynamics of multiple-hole ruptures, especially the interactions between neighboring holes, are less well understood. Here, this study reveals that when two holes ‘meet’ on a curved film, the film evolves into a spinning twisted ribbon before breaking into droplets, distinctly different from what occurs on flat films. We explain the formation and evolution of the spinning twisted ribbon, including its geometry, corrugations, ligaments, and orbits, and compare the experimental observations with models. We compare and contrast this phenomena with its counterpart on planar films. While our experiments are based on the multiple-hole ruptures in corona splash, the underlying principles are likely applicable to other systems. This study sheds light on understanding and controlling droplet formation in multiple-hole rupture, improving public health, climate science, and various industrial applications.

1. Introduction

The rupture of liquid films has been extensively researched, with various studies focusing on different aspects of the process. While many studies investigate the mechanisms preceding the rupture (Thoroddsen *et al.* 2006; Vernay *et al.* 2015; Lo *et al.* 2017; Oratis *et al.* 2020; Duchemin & Josseland 2020; Poulain & Carlson 2022; Sprittles *et al.* 2023), others focus on the mechanisms following it—notably, the rupture of a liquid film produces a large number of droplets, which can be detrimental or beneficial depending on their application (Debrégeas *et al.* 1995; Villermaux 2007; Lhuissier & Villermaux 2009; Bird *et al.* 2010; Feng *et al.* 2014; Villermaux 2020; Jiang *et al.* 2022, 2024). This is crucial in various fields, including disease

† Email address for correspondence: hauyung.lo@kaust.edu.sa, sigurdur.thoroddsen@kaust.edu.sa

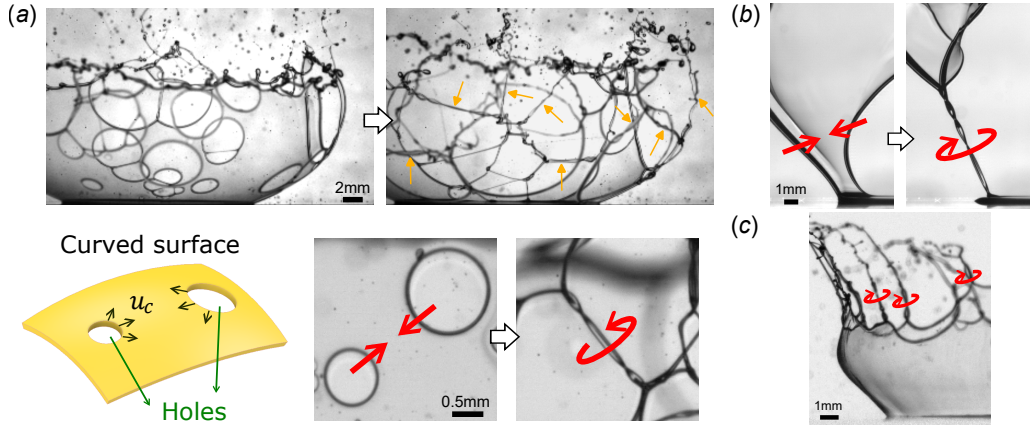


Figure 1: Examples of spinning twisted ribbons appearing on rupturing curved liquid sheets under various scenarios: (a) meeting of two expanding holes, (b) meeting of two edges, (c) spikes of the crown splash. See Movies 1-4.

transmission, aerosol formation, spray drying nanodrugs, oil dispersal, inkjet printing, and spray coating, which in turn affect health, climate, and many industrial applications.

Film rupture can be classified into two categories: single-hole rupture and multiple-hole rupture. In a single-hole rupture, only one hole forms within the timescale of the film's complete collapse (Debrégeas *et al.* 1995; Bird *et al.* 2010; Feng *et al.* 2014; Jiang *et al.* 2022). This scenario is often observed when an external object punctures the film, such as bursting a bubble with a needle. In contrast, multiple-hole rupture involves the formation of several holes either simultaneously or in close succession. This typically occurs in thin, unstable films, where holes nucleate spontaneously at different points. Multiple-hole rupture is likely when the liquid contains a dispersed phase, such as emulsions, air bubbles, or solid suspensions. It is also likely to occur when the liquid film is expanding and thus thinning rapidly. Examples include bag break-up of falling raindrop (Villermaux & Bossa 2009), rapid expansion of bubble (Vledouts *et al.* 2016), bursting of surface bubble (Qian *et al.* 2023), corona splash (Thoroddsen *et al.* 2006; Aljedaani *et al.* 2018), fan spray nozzle (Dombrowski & Fraser 1954), drop impact on small surface (Vernay *et al.* 2015), drop impact on superhydrophobic substrate (Kim *et al.* 2020), and the trapped air film of drop impact onto a pool (Thoroddsen *et al.* 2012).

The multiple-hole rupture cannot be explained simply as a superposition of single-hole ruptures, because the holes interact with each other. Significant progress has been made recently in understanding hole-hole interactions on planar films (Néel *et al.* 2020; Agbaglah 2021; Tang *et al.* 2024). When two holes collide at high Reynolds number, a transverse lamellar sheet emerges and breaks into smaller droplets in a process known as rim-splashing (Néel *et al.* 2020; Tang *et al.* 2024). The droplet formation is closely related to the ligament growth, which has been studied in detail recently on expanding liquid sheet (Wang *et al.* 2018; Wang & Bourouiba 2021).

In this study, we reveal a phenomenon that is unique to curved films: when two holes meet, the liquid film evolves into a spinning twisted ribbon, as shown in figure 1(a) and Movie 1 & 2, and then droplets are ejected due to the spinning. The ribbon is a tiny helicoid-like structure ($\sim 100 \mu\text{m}$ wide) that spins at a high speed ($\sim 5000 \text{ Hz}$). It can, therefore, be easily overlooked without careful inspection. Nevertheless, this phenomenon may have been observed as early as 1954 by Dombrowski and Fraser (Dombrowski & Fraser 1954), who wrote that '*At the instant before coalescence of the two rims, the ribbon of liquid between them may twist*'.

To the best of our knowledge, however, the twisted ribbon has not been studied until now. Besides the meeting of two holes, the twisted ribbon is a general feature that also emerges in various similar systems, such as the meeting of two edges (figure 1*b* and Movie 3) and the spikes in corona splash (figure 1*c* and Movie 4). The analysis is based on experiments of multiple-hole rupture in corona splash, we explain the formation and evolution of spinning twisted ribbons. The underlying principle are likely applicable to other systems where twisted ribbons appear.

2. Experimental methods

Our experimental method is outlined as follows: We observe the ruptures appearing in the corona splash, induced by the high-speed impact of drops on glass slides coated with a thin liquid film (Thoroddsen *et al.* 2006; Aljedaani *et al.* 2018; Sykes *et al.* 2023; Sanjay *et al.* 2023; Tian *et al.* 2024; Khan *et al.* 2024). The crown of the corona splash is a curved liquid film with a thickness of $\sim 10 \mu\text{m}$, the measurement details are provided in the Results section. The multiple-hole rupture of the film is triggered either by tiny air bubbles trapped inside or by its collisions with surrounding fine droplets (Thoroddsen *et al.* 2006; Aljedaani *et al.* 2018). The drop shape is flattened due to aerodynamics stress at high falling speeds. The drops impact at speeds $U=6.4\text{-}8.1 \text{ m/s}$, with vertical diameters $D_V=2.3\text{-}3.7 \text{ mm}$, and horizontal diameters $D_H=3.5\text{-}4.8 \text{ mm}$. The drops are prepared using either silicon oil or glycerol-water mixture, with viscosities of 30-50 cSt and surface tensions of 21 or 65 mN/m.

The curved film (i.e. the crown of corona splash) originates from the liquid in the drop, rather than from the liquid film coated on the glass slides. Therefore, the liquid properties of the coated film do not affect the ruptures directly: the coated film on the glass slides consists of either silicon oil with a viscosity of 1.5 cSt and a thickness of $53 \mu\text{m}$ or ethanol with a thickness of $35 \mu\text{m}$. The film thickness is calculated from the volume of the deposited liquid and the area of the substrate.

We record the impact processes using one or two high-speed cameras, with a frame rate of 31,000 fps and a resolution of $14.5 \mu\text{m}/\text{pixel}$. On a curved surface, the plane of ruptures may not be parallel to the image plane of the camera, leading to parallax errors in length. We correct the parallax error on the curved surface by using the method outlined in the Appendix A. To focus on the dynamics of the ruptures, we present the data in a moving inertial frame that offsets the linear motion of the liquid film.

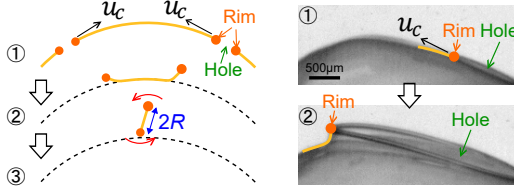
3. Results and Discussion

3.1. Spinning twisted ribbon formation

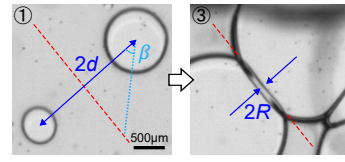
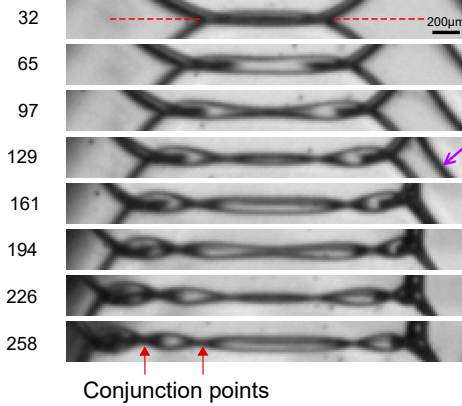
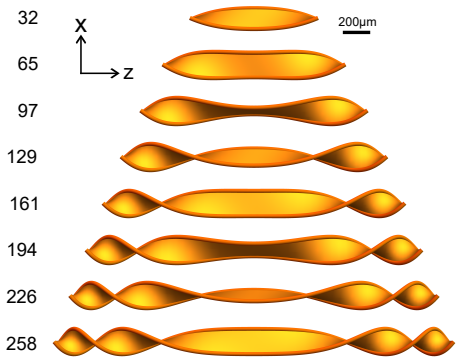
We consider a curved liquid sheet that has developed two holes, as illustrated in figure 2(*a*). The holes expand at a constant speed, known as the Taylor-Culick velocity, given by $u_c = \sqrt{2\gamma/\rho\delta}$, where γ is the surface tension, ρ is the density of the liquid, and δ is the thickness of the sheet. As the holes expand, the displaced fluid accumulates at the circular rim of the liquid sheet, while the thickness of the rest of the sheet remains constant (Savva & Bush 2009). We measure the speed of hole expansions in our experiments (see Appendix B for details). The speed is constant over time as expected. The film thickness is deduced from the measured speed by inverting the Taylor-Culick relation. The thickness varies slightly across different samples as the crown expands and thins with time, with a mean of $7.8 \pm 1.3 \mu\text{m}$ for the silicone oil.

As the two holes expand, they will eventually meet. If the liquid sheet is planar instead of curved, it has been shown that the rims will collide head-on, producing lamella and ejecta

(a) Cross-section of curved liquid sheet



(b) Front view

(c) Time (μs)(d) Time (μs)

(e) Rotated view



Figure 2: The formation mechanism of the spinning twisted ribbon. (a) Considering a curved liquid sheet with two holes that have punctured at slightly different times. Their rims expand at the Taylor-Culick velocity u_c , as indicated by the arrows. The trajectories of the rims deviate from the initial curved surface, because the centripetal force is insufficient to keep the rims on track. The circled numbers indicate the sequence of events. A single hole example is given here and in Movie 5. (b) Consequently, the rims cross each other laterally and begin spinning. See also Movie 2. The distance between the two rupture centers is $2d$. The rotation radius is R . The angle measured from the center-to-center line (blue) is β . The rotation axis is denoted by the red dashed line. (c, d) Magnified video frames of the spinning twisted ribbon and the corresponding predicted surfaces, showing the region of interest along the rotation axis (red dashed line in (b)). The surfaces are plotted by the model in equations (3.1), using the measured parameters $u_c=2.69$ m/s, $d=1.08$ mm, $R=0.09$ mm. No fitting parameters are involved. See also Movie 6. (e) Rotated view of the last plotted ribbon surface in (d).

when the collision speed is sufficient high (Néel *et al.* 2020; Tang *et al.* 2024). On a curved liquid sheet, in contrast, the rims cross each other laterally, as demonstrated in Movie 2 and figure 2(a, b). This occurs because the trajectories of the rims deviate from the initial curved surface, there is insufficient centripetal force to keep them on track, as illustrated in figure 2(b) and Movie 5.

Note that a head-on collision can still happen on a curved substrate in the following scenarios. First, when the two holes are close to each other, the effect of curvature is insignificant. Second, the two holes rupture simultaneously, resulting in a mirror symmetric system. This symmetry leads to an angled head-on collision.

The spinning twisted ribbon is formed after the rims crossing laterally. Due to the attractive surface tension of the connecting liquid sheet, the rims rotate around the axis where they cross laterally, indicated by the dashed red line in figure 2(b-c), forming the spinning twisted ribbon, as shown in Movie 2 and figure 2(c). We define $t = 0$ as the moment that the rims cross laterally for the first time.

We identify several key features of the twisted ribbon from the video images. The ribbon looks similar to a helicoid, but strictly speaking it is not. The ribbon exhibits mirror symmetry

with respect to the central point. There are several points of conjunction (red arrows in figure 2c), where the two rims align along the same line of sight, visually overlapping but not physically touching. The angular distance between neighboring conjunction points is either 0 or π . The number of conjunction points increases over time, indicating more twisting of the sheet. In addition, the spacing between conjunction points is not uniform, they are closer for points located further outward along the axis.

We propose a kinematic model with several idealized assumptions to explain the key features of the spinning twisted ribbon. The predicted structures from the model are shown in figure 2(d) and Movie 6, and compared with the data in figure 2(c). The parameters involved are defined in figure 2(a-b) and elaborated by the supplementary drawing in figure 8 in the Appendix C. In this kinematic model, we consider two horizontal circular holes, either of same size or with one significantly larger than the other. The rims of the holes are expanding horizontally at Taylor-Culick speed u_c . We only consider segments of the rims that the angle β is within the range $-\pi/4 \leq \beta \leq \pi/4$. When an element of the rims reaches the conjunction plane (YZ plane), it rotates around a rotation axis (z -axis) with rotation radius R , angular speed $\omega = u_c \cos \beta / R$, and axial speed $u_z = u_c \sin \beta$. For simplicity, here we take the rotation radius R as a constant, implying a circular closed orbit. The actual non-circular open orbit is presented later with the central force model. Because different parts of the rims reach the conjunction plane at different time, there is a phase lag in time of $\tau(\beta) = d/(u_c \cos \beta) - d/u_c$, where d is the distance between the rotation axis and rupture point. Finally, we assume that the twisted ribbon is a ruled surface formed by connecting two rims. Therefore, the surface of the twisted ribbon is described by the parametric equations (see Appendix C for detailed derivation).

$$\begin{aligned} x(\alpha, \beta) &= \alpha R \cos \left(\frac{u_c t + d}{R} \cos \beta - \frac{d}{R} \right) \\ y(\alpha, \beta) &= \alpha R \sin \left(\frac{u_c t + d}{R} \cos \beta - \frac{d}{R} \right) \\ z(\beta) &= (u_c t + d) \sin \beta \end{aligned} \tag{3.1}$$

where $-1 \leq \alpha \leq 1$, $-\beta_0 \leq \beta \leq \beta_0$, and $\cos \beta_0 = d/(u_c t + d)$ with $\beta_0 \in [0, \pi/2]$. This surface is plotted in figure 2(d) using measured parameters $u_c = 2.69$ m/s, $d = 1.08$ mm, and $R = 0.09$ mm. The predicted surfaces agree well with the experimental data in figure 2(c), reproducing the key features discussed above. No fitting parameters are involved. We have artistically added a thick circular rim to the edge of the surface, the thick rim is not included in the equations.

Note that the model only considers two holes, while in the experiments more than two holes frequently occur, affecting the shape of the twisted ribbon. For example, see the third rim on the right-hand side in figure 2(c).

We predict that the mean curvature of the twisted ribbon should be very small for two reasons: First, from the perspective of pressure balance, it has been suggested that the pressure across the film can be equilibrated quickly after ruptures at the timescale of 10 μ s (Bird *et al.* 2010). Second, from the perspective of geometry, the shape of the twisted ribbon looks similar to a helicoid, which is a well-known minimal surface. We calculate the mean curvature of the surfaces described by equation (3.1) (see Appendix D for details). We find that the upper bound of the mean curvature is $H < \frac{1}{d}$, which is relatively small when comparing the hole-axis distance d with the rotation radius R . Typically, the R is on the order of 100 μ m, while d is on the order of 1 mm, such that $d > 10R$. On the contrary, if d were small, this phenomenon would not occur in the first place, as the surface would

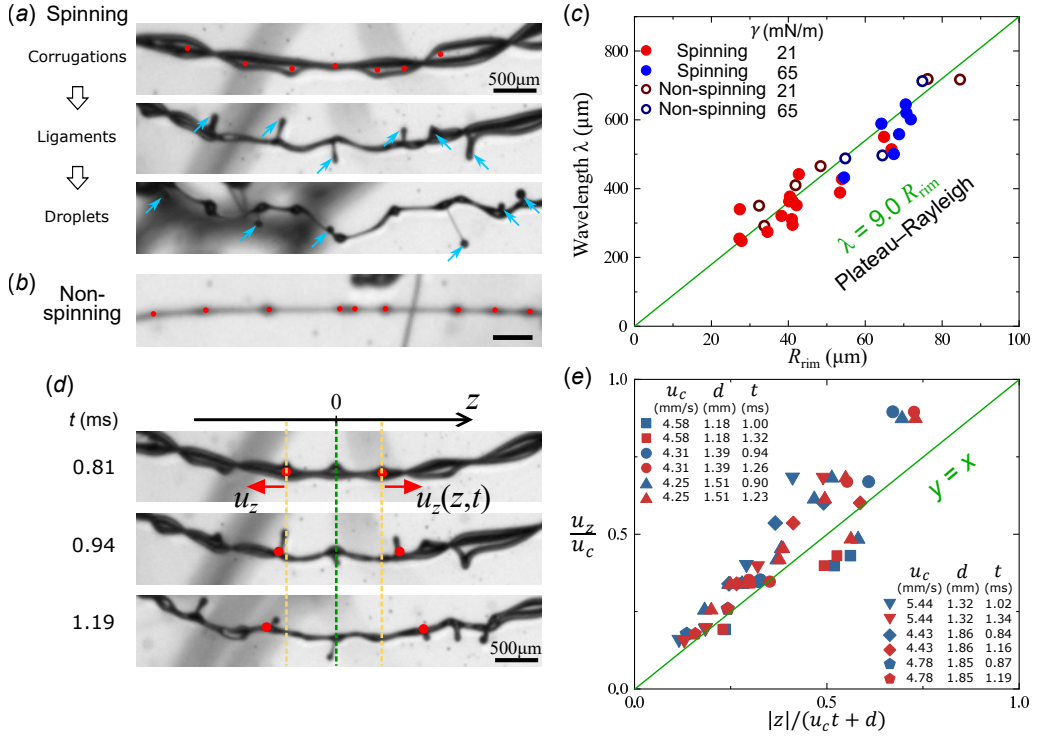


Figure 3: Corrugations and ligaments. (a) The corrugations on the rims are marked by the red dots. The ligaments are marked by the cyan arrows. Corrugations grow into ligaments, pinch-off, and eject secondary droplets due to the spinning. (b) For the non-spinning case, the corrugations do not grow into ligaments. (c) The wavelength λ is calculated by dividing the length of a segment by the number of corrugations it contains. The measured wavelength λ agree with the expected wavelength of Plateau-Rayleigh instability (green line) for both spinning (solid dots) and non-spinning (open dots) conditions at different rim radius R_{rim} and surface tensions γ . (d) Snapshots of the twisted ribbon at different time. The corrugations and ligaments (red dots) are moving outward with speed u_z relative to the center ($z = 0$) of the twisted ribbon, confirming the existence of the outward axial flow. (e) The speed of the outward axial flow u_z measured at different conditions as shown in the legend. See also Movie 7.

be approximately flat instead of curved. Therefore, the mean curvature of the ribbon is very small as expected, and the appearance of a helicoid-like ribbon is reasonable.

3.2. Corrugations and ligaments

Next, we observe that the rims become unstable during spinning at later times, forming corrugations along their lengths that grow into ligaments, which pinch off and eject secondary droplets, as shown in Movie 7 and figure 3(a). The corrugations are marked by red dots. The ligaments are marked by cyan arrows. Nevertheless, the instability is not uniquely associated with spinning. Similar corrugations are also observed when spinning is absent. Without spinning, however, the corrugations do not grow into ligaments, as shown in figure 3(b).

We can distinguish this phenomenon from the previously discovered rim splashing phenomenon by inspecting Movie 7 and figure 3(a), even though they appear similar in still images (Néel *et al.* 2020; Tang *et al.* 2024). First, unlike in rim-splashing, the two rims of the ribbon have not coalesced when the ligaments develop. Second, in rim splashing, the ligaments are straight and perpendicular to the film. For the spinning ribbon, in contrast, the ligaments are rotating with the ribbon. For example, the center ligament in Movie 7 has been rotated by $\sim 180^\circ$. Third, under spinning conditions, ligaments that break up into

droplets are observed at a Weber number lower than that in rim splashing on planar surface. By convention, the Weber number is defined as $We = \rho(2u_c)^2(2R_{\text{rim}})/\gamma$ and $We \sim 58$ here. In comparison, for the rim splashing, ligaments that break up into droplets are observed at $We > 120$. Although we have not yet explored the threshold Weber number, the data suggest that ligaments and droplets can be produced at a lower Weber number in this rim spinning case compared to the rim splashing case.

We plot the wavelength of the instability, λ , against the rim radius, R_{rim} , as shown in figure 3(c). The plot includes data for both spinning and non-spinning conditions for two different surface tensions. The wavelength λ is calculated by dividing the length of a segment by the number of corrugations it contains. The rim radii are measured either just before spinning begins or, for the non-spinning case, just after the two rims coalesce. For all conditions studied here, the data agree with the Plateau-Rayleigh instability that $\lambda = 9.0R_{\text{rim}}$. Therefore, Plateau-Rayleigh instability leads to corrugations, while the spinning motion is also essential for the formation of ligaments that pinch off into droplets.

The corrugations and ligaments are moving outward with speed u_z relative to the center ($z = 0$) of the twisted ribbon, as indicated in figure 3(d), confirming the existence of the outward axial flow. Experimentally, u_z is measured by tracking the positions of corrugations over time. By equations (3.1), the axial flow speed u_z is given by

$$\frac{u_z(z, t)}{u_c} \equiv \frac{1}{u_c} \left| \frac{dz}{dt} \right| = \frac{|z|}{u_c t + d} \quad (3.2)$$

This relation agrees with experimental data as shown in figure 3(e). It is interesting that, by volume conservation, the outward flow would reduce the thickness of the sheet and the rim. Unfortunately, the resolution in our experiments is insufficient to quantify this change in thickness directly.

The mechanisms of ligament growth and droplet formation have been studied by Wang and Bourouiba in a similar system of expanding liquid sheet, finding a criterion that the Bond number $Bo = 1$ as long as the local Reynolds number $Re \gtrsim 8$ (Wang *et al.* 2018; Wang & Bourouiba 2021). In our experiment, however, $Re \sim 1$, which falls outside the application range of this theory.

3.3. Two-body central force model

Finally, we elucidate the ‘orbit’ of the rims of the spinning ribbon by using the classical two-body central force model and direct measurements (Goldstein *et al.* 2011). We previously assumed the orbit was circular for simplicity, but in fact it is open and non-circular. Consider a thin strip of the ribbon with a dumbbell-shaped cross-section, as shown in figure 4(a), where two circular rims are connected by a thin liquid string. The surface tension on the liquid string exerts an attractive central force between the two circular rims. Following the classical treatment, the two-body system is reduced to a one-body system with a relative position $\mathbf{r}(t)$ and a reduced mass per length $m_\mu = \rho\pi r_1^2 r_2^2 / (r_1^2 + r_2^2)$. The magnitude of the central force per length is twice the surface tension γ , accounting for both the upper and lower surfaces of the liquid string.

We experimentally measure the orbits using two high speed cameras positioned at orthogonal angles, and then compare them with the theoretical orbits. A measured orbit is shown in figure 4(b), with additional examples provided in the Appendix E. The dots with error bars represent measured data, and the line shows an interpolated orbit. The colors indicate time progression, ranging from red ($t=0$) to purple ($t=550 \mu\text{s}$). We calculate the orbits, as shown in figure 4(c), by solving the differential equations numerically using *Mathematica* with real liquid properties and measured initial conditions (see figure captions and Appendix E) (Taborek 2010). The experiments agree with numerical calculations semi-

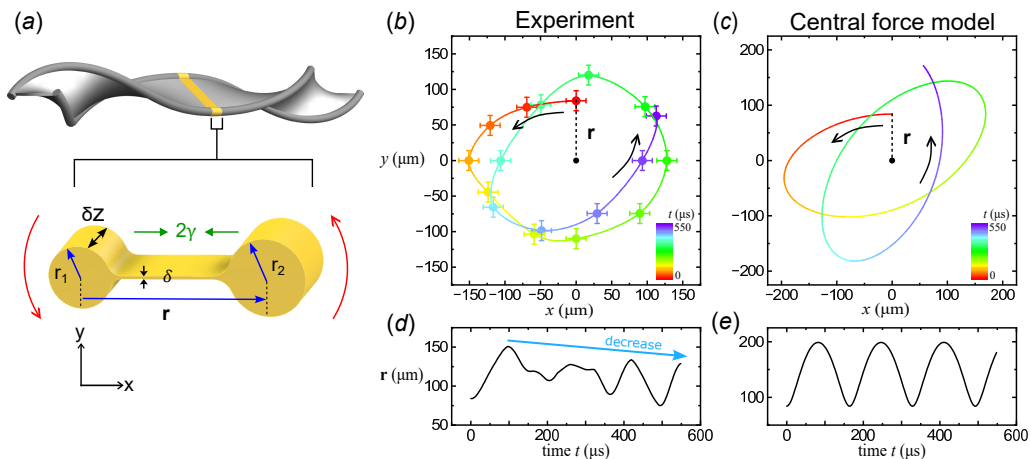


Figure 4: Explain the ribbon’s orbit by the two-body central force model. (a) Sketch of a thin strip of the ribbon with a dumbbell-shaped cross-section. Two circular rims are connected by a thin liquid string, which exerts an attractive central force. (b) Measured orbit, showing the data (dots) and interpolation (line). The colors indicate time progression, ranging from red ($t=0$) to purple ($t=550 \mu\text{s}$). (c) Orbit calculated with measured parameters: $\gamma=20.8 \text{ mN/m}$, $\rho=960 \text{ kg/m}^3$, $r(0)=841 \mu\text{m}$, $v_r(0)=0$, $v_\theta(0)=4.45 \text{ m/s}$, $m_\mu=586 \mu\text{g/m}$. The data agree with the model semi-quantitatively. (d, e) The plots of $\mathbf{r}(t)$ reveal that the measured orbit is shrinking over time. Additional examples are presented in the Appendix E.

quantitatively, revealing similar non-circular open orbits. The main discrepancy is that the size of the measured orbit is smaller and shrinks over time, as highlighted by the downward trend of $\mathbf{r}(t)$ in figure 4(d), which is inconsistent with the model. We believe the shrinking of the orbit is due to the air resistance and the variation in mass of the rims over time, which in turn is due to internal fluid flow caused by the previously discussed Plateau-Rayleigh instability (figure 3a-b), outward axial flow (figure 3c-d), and the centrifugal force. Moreover, by replacing the constant R in equations (3.1) with $\mathbf{r}(t)/2$, the kinematic model is generalized to account for non-circular open orbits. Therefore, the ribbon’s rotation is explained by the two-body central force model satisfactorily, but further studies on the internal fluid flow could improve the model’s accuracy.

This system presents an unusual scenario that the central force is distance-independent (potential is linear), in contrast to the typical celestial orbits (inverse square law) and harmonic oscillators (Hooke’s law). Other examples of systems with linear potential include the triangular quantum well in high-electron-mobility transistor (Harrison & Valavanis 2016, p. 116) and the quark confinement in mesons (Griffiths 2020, p. 173).

4. Conclusion

To conclude, we have explained the formation and evolution of spinning twisted ribbons. The ribbon forms when the rim deviates from the original curved surface due to insufficient centripetal force. This phenomenon is unique to curved films and does not occur in planar films. The geometry and motion of the ribbons are described by the kinematic model and the central force model. The helicoid-like structure of the ribbon is consistent with its small mean curvature. During spinning, the rims’ corrugations grow into ligaments, which pinch off and eject secondary droplets. These corrugations arise from the Plateau-Rayleigh instability. This rim-spinning phenomenon is distinctly different from the rim-splashing observed in previous studies, including its facilitation of droplet formation at lower Weber numbers. We demonstrate that the ribbon contains an intrinsic outward axial flow, which may lead to

variations in rim thickness during spinning. The orbit of the spinning ribbon is open and non-circular, as predicted by the central force model. However, the experimentally observed orbit shrinks over time, which is inconsistent with our model. We attribute this discrepancy to variations in the mass of the rims during spinning. While this study focuses on experiments of multiple-hole rupture in corona splash, the underlying principles are likely applicable to other systems where twisted ribbons emerge.

Supplementary data. Supplementary movies are available at

Acknowledgements. We acknowledge Vivek Mugundhan, Andres Aguirre-Pablo, Krishna Dharmarajan, Marcus Lin, Ziqiang Yang, Abdullah Alhareth, Farrukh Kamoliddinov, Moaz Kattoah for their help in experiments and fruitful discussions.

Funding. This work is financially supported by King Abdullah University of Science and Technology (KAUST) under grants number URF/1/2621-01-01 and BAS/1/1352-01-01.

Declaration of interests. The authors report no conflict of interest.

Data availability statement. All data is included in the manuscript and supplementary data.

Author ORCIDs. Authors may include the ORCID identifiers as follows. J.H.Y.Lo, <https://orcid.org/0000-0001-9633-4862>; Y.Liu, <https://orcid.org/0000-0001-6107-7560>; T.Alghamdi, <https://orcid.org/0000-0003-0602-337X>; M.F.Afzaal, <https://orcid.org/0000-0002-8304-9795>; S.T.Thoroddsen, <https://orcid.org/0000-0001-6997-4311>

Author contributions. S.T.T conceived the project; T.A., J.H.Y.L, and Y.L. built the experimental setup; J.H.Y.L, Y.L., and S.T.T performed the experiments; J.H.Y.L, Y.L., and S.T.T analyzed the data; J.H.Y.L and Y.L. constructed the models; J.H.Y.L and M.F.A performed the numerical simulations; J.H.Y.L, Y.L., and S.T.T wrote the manuscript.

Appendix A. Correction of parallax error

On a curved surface, the plane of ruptures may not be parallel to the image plane of the camera, inducing errors in length measurements. We correct these parallax errors by the following method:

First, we use the side view image to measure the local rotation angles (Euler angles) θ and ϕ , as shown in figure 5. The angle ϕ is read from the image directly, while the angle θ is obtained, assuming axisymmetry, from the equation $\sin \theta = s/R$, where R is the horizontal radius of the crown, s is the distance of the plane from the center. A top view drawing is provided in figure 5 for clarity.

Next, we derive the formula to correct for the parallax errors in length measurements. The rotation matrix is

$$\mathbf{R} = \begin{pmatrix} 1 & 0 & 0 \\ 0 & \cos \phi & -\sin \phi \\ 0 & \sin \phi & \cos \phi \end{pmatrix} \begin{pmatrix} \cos \theta & 0 & \sin \theta \\ 0 & 1 & 0 \\ -\sin \theta & 0 & \cos \theta \end{pmatrix} = \begin{pmatrix} \cos \theta & 0 & \sin \theta \\ \sin \theta \sin \phi & \cos \phi & -\cos \theta \sin \phi \\ -\cos \phi \sin \theta & \sin \phi & \cos \theta \cos \phi \end{pmatrix}, \quad (\text{A } 1)$$

while the projection matrix is

$$\mathbf{P} = \begin{pmatrix} 1 & 0 & 0 \\ 0 & 1 & 0 \\ 0 & 0 & 0 \end{pmatrix}. \quad (\text{A } 2)$$

Let $\mathbf{d} \equiv \begin{pmatrix} d_x \\ d_y \\ 0 \end{pmatrix}$ be an arbitrary unit line on a plane, then $\mathbf{d}' \equiv d' \begin{pmatrix} \cos \psi \\ \sin \psi \\ 0 \end{pmatrix}$ is the rotated and

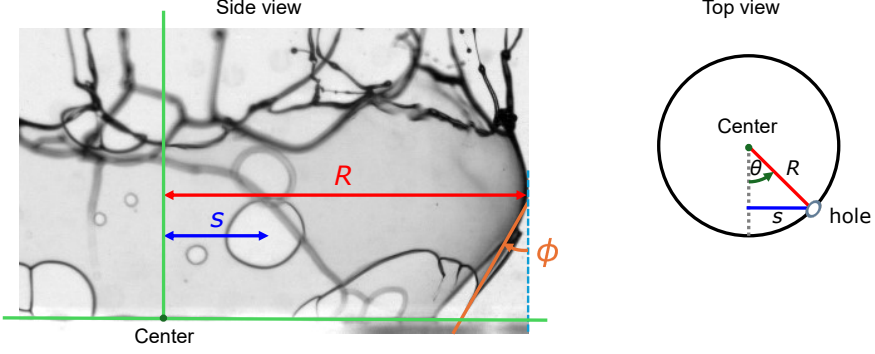


Figure 5: Side and top views for parallax corrections.

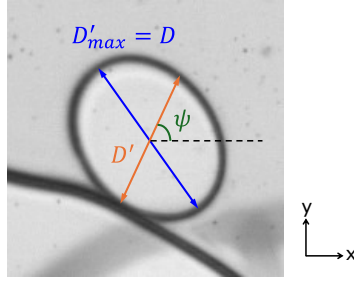


Figure 6: Image used to verify the parallax correction and equation (A4).

projected line from $\mathbf{d}' = \mathbf{PRd}$. We then get

$$\begin{aligned} d_x &= d' \cos \psi \sec \theta \\ d_y &= d' (\sin \psi \sec \phi - \cos \psi \tan \theta \tan \phi) . \end{aligned} \quad (\text{A } 3)$$

Therefore, the ratio of the length before and after this transformation is

$$\Psi(\psi) = \frac{|\mathbf{d}|}{|\mathbf{d}'|} = \frac{d_x^2 + d_y^2}{d'^2} = \sqrt{\left(\frac{\cos \psi}{\cos \theta}\right)^2 + \left(\frac{\sin \psi}{\cos \phi} - \cos \psi \tan \theta \tan \phi\right)^2} \quad (\text{A } 4)$$

where Ψ is the ratio between the real length, d , and the apparent length, d' . In other words, we can deduce the real length from the apparent length by $d = \Psi d'$.

To verify equation (A4), we test it on the diameter of a hole. We make use of the facts that: 1) physically, the capillary-driven hole is circular, and 2) the apparent length of the longest axis of the transformed hole, D'_{max} , is the real diameter of the hole, D . Experimentally, we measure $D'_{max} = D$ and the width of the hole along an arbitrary axis, D' , as shown in figure 6. We calculate the ratio D/D' and compare it with the ratio Ψ deduced by A4. In the example in figure 6, for $\psi = 59.5^\circ$, $\theta = -33.6^\circ$, $\phi = 27.5^\circ$, we get $D/D' = 1.256$ and $\Psi = 1.259$. The measured ratio and the calculated ratio are very close, verifying that equation (A4) is correct.

Appendix B. Measured Taylor-Culick speed and corresponding film thickness

It is well known that the hole expansion follows the Taylor-Culick speed. In our experiments, we measure the velocity from the relative position between two rims r versus time t , after the parallax corrections described above, as shown in figure 7. We can see that r decreases

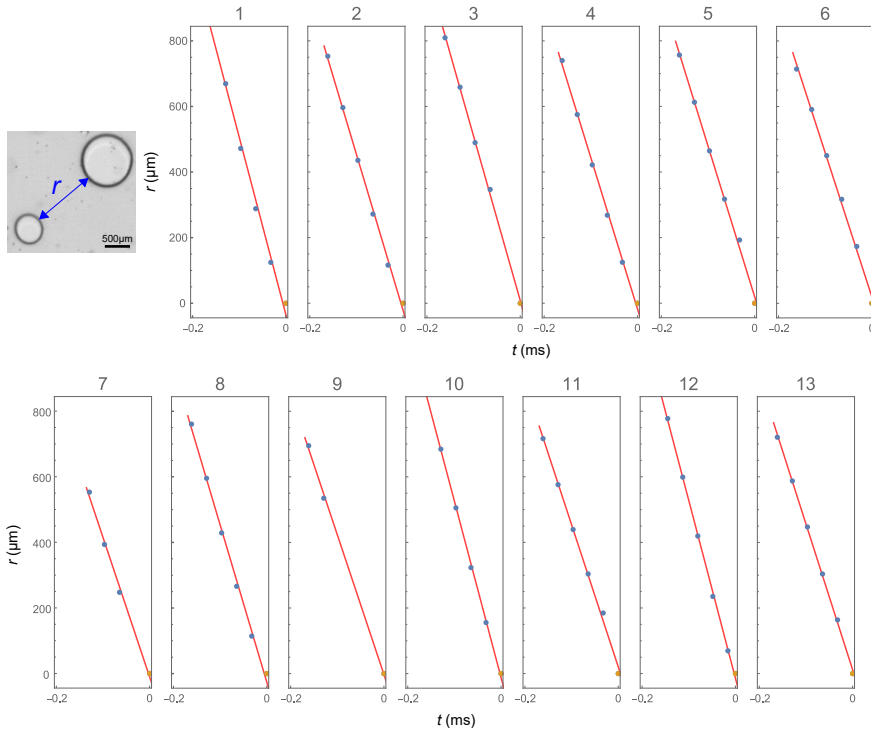


Figure 7: The nearest distance between two holes versus time for samples #1-13. The Taylor-Culick speed is deduced from the slope.

linearly with t as expected. The red lines are the best fit. The thickness of the films is deduced from the measured Taylor-Culick speed using the equation:

$$\delta = \frac{2\gamma}{u_c^2 \rho} \quad (\text{B } 1)$$

where u_c is the Taylor-Culick speed measured from the data, $\gamma = 20.8 \text{ mN/m}$ is the surface tension and $\rho = 960 \text{ kg/m}^3$ is the density of the silicone oil. The calculated thickness varies slightly across different samples as the crown expands and thins with time., with a mean of $7.8 \text{ }\mu\text{m}$ and a standard deviation of $1.3 \text{ }\mu\text{m}$.

In the experiments, a small error on identifying $t = 0$ is induced when the observer (camera) is not perpendicular to the surface.

Appendix C. Derivation of the twisting equations (3.1)

We propose a kinematic model to explain the geometry of the spinning twisted ribbon. The parameters are defined in both figure 2(a-b) in the main text and in figure 8 above. We consider two identical circular rims that are expanding radially at speed u_c from their rupture points along two parallel XZ planes separated by distance $2R$. For convenience, we only consider a segment of a rim where the angle β is within the range $-\pi/4 \leq \beta \leq \pi/4$. The two rims conjunct (relative to an observer at $y \rightarrow \infty$) at a perpendicular YZ plane at the center, such that the distance between the conjunction plane and rupture points is d . We model that when an element of the rims reaches the conjunction plane, it rotates around the z-axis (rotation axis) with rotation radius R , angular speed $\omega = u_c \cos \beta / R$, and axial speed $u_z = u_c \sin \beta$. Because different parts of the rims reach the conjunction plane at different

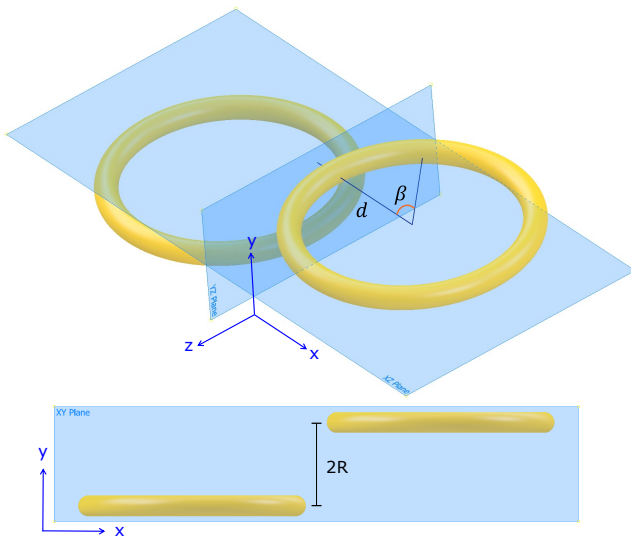


Figure 8: Schematic drawings for the derivation of equations

time, there is a phase lag in arrival time $\tau(\beta) = d/(u_c \cos \beta) - d/u_c$. Therefore, the motion of the rim is described by

$$\begin{aligned}
 x &= R \cos (\omega (t - \tau)) \\
 &= R \cos \left(\frac{u_c \cos \beta}{R} t + \frac{d}{R} \cos \beta - \frac{d}{R} \right) \\
 &= R \cos \left(\frac{u_c t + d}{R} \cos \beta - \frac{d}{R} \right).
 \end{aligned} \tag{C1}$$

Similarly,

$$y = R \sin \left(\frac{u_c t + d}{R} \cos \beta - \frac{d}{R} \right). \tag{C2}$$

From the axial speed $u_z = u_c \sin \beta$, by integration, we get $z = u_c t \sin \beta + z_o$. By definition of t , when $t = 0$, $z = d \sin \beta$, thus $z_o = d \sin \beta$. Therefore,

$$z(\beta) = (u_c t + d) \sin \beta. \tag{C3}$$

Finally, we assume that the twisted ribbon is a ruled surface formed by connecting two rims. By introducing the parameter α , the surface of the twisted ribbon is described by the parametric equations

$$\begin{aligned}
 x(\alpha, \beta) &= \alpha R \cos \left(\frac{u_c t + d}{R} \cos \beta - \frac{d}{R} \right) \\
 y(\alpha, \beta) &= \alpha R \sin \left(\frac{u_c t + d}{R} \cos \beta - \frac{d}{R} \right) \\
 z(\beta) &= (u_c t + d) \sin \beta
 \end{aligned} \tag{C4}$$

where $-1 \leq \alpha \leq 1$, $-\beta_0 \leq \beta \leq \beta_0$. Here the range of β is bounded by β_0 that represents the segment of the rim that has already reached the rotation axis at time t . It is given by $\cos \beta_0 = d/(u_c t + d)$ with $\beta_0 \in [0, \pi/2]$.

Appendix D. Curvature of the twisted ribbon

The mean curvature H of the twisted ribbon is calculated by the formula,

$$H = \frac{eG - 2fF + gE}{2(EG - F^2)} \quad (\text{D } 1)$$

where $\{E, F, G\}$ and $\{e, f, g\}$ are the coefficients of the first and second fundamental form of the surface described by equations (3.1) in the main text. We get

$$H(\alpha, \beta) = \left(\frac{1}{u_{ct} + d} \right) \left(\frac{\alpha}{2(\cos^2 \beta + \alpha^2 \sin^2 \beta)^{3/2}} \right) \quad (\text{D } 2)$$

Numerically, we find that, in the range of interest $-\pi/4 < \beta < \pi/4$, the second term

$$\frac{\alpha}{2(\cos^2 \beta + \alpha^2 \sin^2 \beta)^{3/2}} < 0.55.$$

Therefore, the upper bound of the mean curvature is

$$H < \frac{1}{u_{ct} + d} < \frac{1}{d} \quad (\text{D } 3)$$

Appendix E. Orbit calculation in central force model

Using the two-body central force model, the orbit is obtained by solving the following differential equations numerically by *Mathematica*,

$$\begin{aligned} r''(t) - r(t)\theta'(t)^2 + \frac{2\gamma}{m_\mu} &= 0 \\ r(t)\theta''(t) + 2r'(t)\theta'(t) &= 0 \end{aligned} \quad (\text{E } 1)$$

where $r(t)$ and $\theta(t)$ are the relative distance and angle at time t in polar coordinate system, γ is the surface tension of the liquid sheet, $m_\mu = \rho\pi r_1^2 r_2^2 / (r_1^2 + r_2^2)$ is the reduce mass per length, ρ is the density of the liquid sheet. We also define $v_r(t) \equiv r'(t)$ and $v_\theta(t) \equiv r(t)\theta'(t)$ when specifying the initial conditions. The value of $v_\theta(0)$ is the measured Taylor-Culick speed, i.e. the constant film retraction speed before spinning, as shown in figure 7. The measured and calculated orbits are provided in figure 9 below. The parameters involved in each calculation are presented in the figure caption. Open non-circular orbits are obtained as expected, according to Bertrand's theorem.

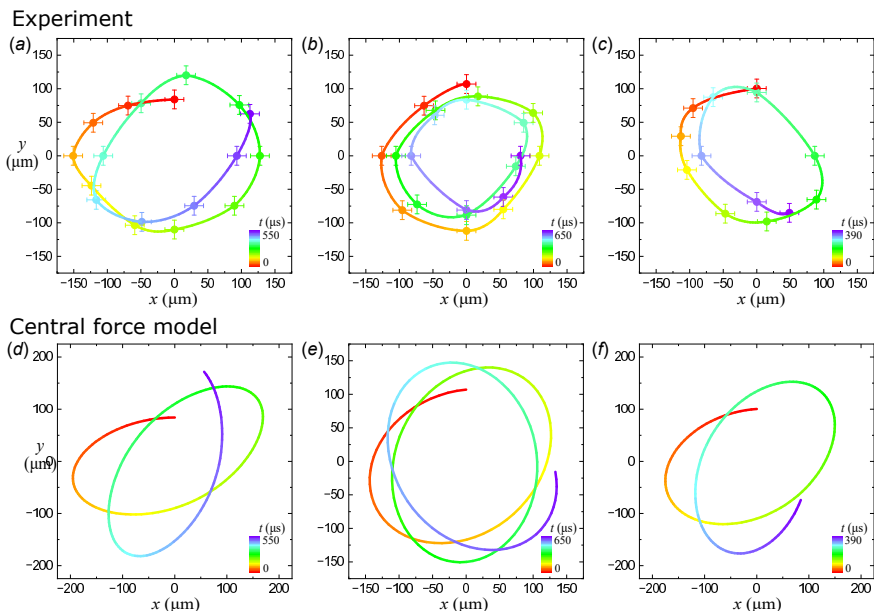


Figure 9: Measured and calculated orbits. (a-c) Experimental data. (d-f) Orbits calculated by solving (E 1) with liquid properties $\gamma=20.8$ mN/m, $\rho=960$ kg/m³, and initial conditions approximated from above measurements: (d) $r(0)=841$ μm , $v_\theta(0)=4.45$ m/s, $v_r(0)=0$, $m_\mu=586$ $\mu\text{g}/\text{m}$. (e) $r(0)=1071$ μm , $v_\theta(0)=4.01$ m/s, $v_r(0)=-0.40$ m/s, $m_\mu=449$ $\mu\text{g}/\text{m}$. (f) $r(0)=1003$ μm , $v_\theta(0)=4.94$ m/s, $v_r(0)=-0.33$ m/s, $m_\mu=397$ $\mu\text{g}/\text{m}$.

REFERENCES

- AGBAGLAH, GG 2021 Breakup of thin liquid sheets through hole-hole and hole-rim merging. *Journal of Fluid Mechanics* **911**, A23.
- ALJEDAANI, ABDULRAHMAN B, WANG, CHUNLIANG, JETLY, ADITYA & THORODDSEN, SIGURDUR T 2018 Experiments on the breakup of drop-impact crowns by marangoni holes. *Journal of Fluid Mechanics* **844**, 162–186.
- BIRD, JAMES C, DE RUITER, RIËLLE, COURBIN, LAURENT & STONE, HOWARD A 2010 Daughter bubble cascades produced by folding of ruptured thin films. *Nature* **465** (7299), 759–762.
- DEBRÉGEAS, G, MARTIN, PASCAL & BROCHARD-WYART, F 1995 Viscous bursting of suspended films. *Physical review letters* **75** (21), 3886.
- DOMBROWSKI, NORMAN & FRASER, REGINALD PERCY 1954 A photographic investigation into the disintegration of liquid sheets. *Philosophical Transactions of the Royal Society of London. Series A, Mathematical and Physical Sciences* **247** (924), 101–130.
- DUCHEMIN, LAURENT & JOSSERAND, CHRISTOPHE 2020 Dimple drainage before the coalescence of a droplet deposited on a smooth substrate. *Proceedings of the National Academy of Sciences* **117** (34), 20416–20422.
- FENG, JIE, ROCHÉ, MATTHIEU, VIGOLO, DANIELE, ARNAUDOV, LUBEN N, STOYANOV, SIMEON D, GURKOV, THEODOR D, TSUTSUMANOVA, GICHKA G & STONE, HOWARD A 2014 Nanoemulsions obtained via bubble-bursting at a compound interface. *Nature physics* **10** (8), 606–612.
- GOLDSTEIN, HERBERT, POOLE, CHARLES & SAFKO, JOHN 2011 *Classical Mechanics*, 3rd edn. Pearson Education.
- GRIFFITHS, DAVID 2020 *Introduction to elementary particles*. John Wiley & Sons.
- HARRISON, PAUL & VALAVANIS, ALEX 2016 *Quantum wells, wires and dots: theoretical and computational physics of semiconductor nanostructures*. John Wiley & Sons.
- JIANG, XINGHUA, ROTILY, LUCAS, VILLERMAUX, EMMANUEL & WANG, XIAOFEI 2022 Submicron drops from flapping bursting bubbles. *Proceedings of the National Academy of Sciences* **119** (1), e2112924119.
- JIANG, XINGHUA, ROTILY, LUCAS, VILLERMAUX, EMMANUEL & WANG, XIAOFEI 2024 Abyss aerosols: Drop production from underwater bubble collisions. *Physical Review Letters* **133** (2), 024001.

- KHAN, TALHA, JIN, ZHEYAN & YANG, ZHIGANG 2024 Impact dynamics of non-spherical droplets on a thin water film. *Physics of Fluids* **36** (3).
- KIM, SEUNGHO, WU, ZIXUAN, ESMAILI, EHSAN, DOMBROSKIE, JASON J & JUNG, SUNGHWAN 2020 How a raindrop gets shattered on biological surfaces. *Proceedings of the National Academy of Sciences* **117** (25), 13901–13907.
- LHUISSIER, HENRI & VILLERMAUX, EMMANUEL 2009 Bursting bubbles. *Physics of Fluids* **21** (9).
- LO, HAU YUNG, LIU, YUAN & XU, LEI 2017 Mechanism of contact between a droplet and an atomically smooth substrate. *Physical Review X* **7** (2), 021036.
- NÉEL, B, LHUISSIER, HENRI & VILLERMAUX, E 2020 ‘fines’ from the collision of liquid rims. *Journal of Fluid Mechanics* **893**, A16.
- ORATIS, ALEXANDROS T, BUSH, JOHN WM, STONE, HOWARD A & BIRD, JAMES C 2020 A new wrinkle on liquid sheets: Turning the mechanism of viscous bubble collapse upside down. *Science* **369** (6504), 685–688.
- POULAIN, STÉPHANE & CARLSON, ANDREAS 2022 Droplet settling on solids coated with a soft layer. *Journal of Fluid Mechanics* **934**, A25.
- QIAN, HONGTAO, YANG, ZHENGYU, ZHANG, XIAOFEI, FENG, JIE & LI, CHENG 2023 Dilute oil-in-water emulsion initiates multiple holes formation during bubble bursting. *International Journal of Multiphase Flow* **167**, 104525.
- SANJAY, VATSAL, LAKSHMAN, SRINATH, CHANTELOT, PIERRE, SNOEIJER, JACCO H & LOHSE, DETLEF 2023 Drop impact on viscous liquid films. *Journal of Fluid Mechanics* **958**, A25.
- SAVVA, NIKOS & BUSH, JOHN WM 2009 Viscous sheet retraction. *Journal of Fluid Mechanics* **626**, 211–240.
- SPRITTLES, JAMES E, LIU, JINGBANG, LOCKERBY, DUNCAN A & GRAFKE, TOBIAS 2023 Rogue nanowaves: A route to film rupture. *Physical Review Fluids* **8** (9), L092001.
- SYKES, THOMAS C, CIMPEANU, RADU, FUDGE, BEN D, CASTREJÓN-PITA, J RAFAEL & CASTREJÓN-PITA, ALFONSO A 2023 Droplet impact dynamics on shallow pools. *Journal of Fluid Mechanics* **970**, A34.
- TABOREK, PETER 2010 *Mathematica Handbook*. Anteater ePress.
- TANG, KAITAO, ADCOCK, TAA & MOSTERT, WOUTER 2024 Fragmentation of colliding liquid rims. *Journal of Fluid Mechanics* **987**, A18.
- THORODDSEN, ST, ETOH, T GOJI & TAKEHARA, K 2006 Crown breakup by Marangoni instability. *Journal of Fluid Mechanics* **557**, 63–72.
- THORODDSEN, SIGURDUR T, THORAVAL, M-J, TAKEHARA, K & ETOH, TG 2012 Micro-bubble morphologies following drop impacts onto a pool surface. *Journal of fluid mechanics* **708**, 469–479.
- TIAN, YUAN SI, ALJEDAANI, ABDULRAHMAN B, ALGHAMDI, TARIQ & THORODDSEN, SIGURDUR T 2024 Dancing ejecta. *Journal of Fluid Mechanics* **981**, A4.
- VERNAY, CLARA, RAMOS, LAURENCE & LIGOURE, CHRISTIAN 2015 Bursting of dilute emulsion-based liquid sheets driven by a marangoni effect. *Physical Review Letters* **115** (19), 198302.
- VILLERMAUX, EMMANUEL 2007 Fragmentation. *Annu. Rev. Fluid Mech.* **39** (1), 419–446.
- VILLERMAUX, EMMANUEL 2020 Fragmentation versus cohesion. *Journal of Fluid Mechanics* **898**, P1.
- VILLERMAUX, EMMANUEL & BOSSA, BENJAMIN 2009 Single-drop fragmentation determines size distribution of raindrops. *Nature physics* **5** (9), 697–702.
- VLEDOUTS, A, QUINARD, J, VANDENBERGHE, N & VILLERMAUX, E 2016 Explosive fragmentation of liquid shells. *Journal of Fluid Mechanics* **788**, 246–273.
- WANG, Y & BOUROUIBA, L 2021 Growth and breakup of ligaments in unsteady fragmentation. *Journal of Fluid Mechanics* **910**, A39.
- WANG, Y, DANDEKAR, R, BUSTOS, N, POULAIN, S & BOUROUIBA, L 2018 Universal rim thickness in unsteady sheet fragmentation. *Physical review letters* **120** (20), 204503.